Photometric Phase Functions of Resident Space Objects and Space Debris Extracted from Brightness Measurements

Jiří Šilha, Peter Jevčák, Matej Zigo, Tomáš Hrobár, András Szilágyi-Sándor
Faculty of Mathematics, Physics and Informatics, Comenius University, Bratislava, Slovakia

ABSTRACT

Space object characterization is a methodology essential for understanding the object's origin and its threat to the space environment. It is often conducted by ground based optical sensors by acquiring photometric data. Photometry is a commonly used method to extract physical and dynamical (rotation) properties of space objects, such as asteroids or variable stars. Usually, it consists of the processing and analysis of light curves and rotational functions. Such measurements help to categorize space objects to the groups according to similarities in surface properties and characteristics, reveal some specific spectral features related to certain materials in comparison to laboratory samples or find evidence and rate of space weather effects. In our work we present the data reduction of light curves extracted from the publicly available photometric catalogues such as Mini-MegaTORTORA (MMT) catalogue and Space Debris Light Curve Catalogue (SDLCD), which combined contain light curves for more than 10 000 Resident Space Objects (RSOs) including functional satellites and space debris objects. For more than 600 rotating objects including upper stages, non-functional spacecraft, and debris fragments we constructed the phase functions and along with them also estimated parameters β and mean cross section multiplied by geometric albedo. For objects with known dimensions, such Titan 3A Transtage R/B we additionally extracted the mean geometric albedo values as a function of time. We report our findings, as well as the physical parameters estimated for the analyzed objects distinguishing upper stages, spacecraft and fragmentation debris objects.

1. INTRODUCTION TO PHASE FUNCTIONS

1.1 Minor planets

To better understand the problem of phase functions and their interpretation we discuss phase functions of natural objects. Phase functions help to understand the asteroid's surface properties such as porosity, roughness, particle size, complex refractive index etc. In an asteroid community phase function is defined by several parameters including absolute magnitude H which is visual brightness of the object in Johnson V filter when observed 1 Astronomical Unit (1 AU) from the observer and the Sun under 0° phase angle ϕ. Phase angle ϕ is an angle between the sun-object and observer. Parameter H defines the intrinsic brightness of an asteroid and its dependence on the object's size and albedo. Another parameter which defines the phase function is so-called slope factor G which describes the shape of the phase function [1]. For natural objects such as asteroids phase functions usually show linear decrease for phase angle larger than 4-5° while for lower phase angles sudden increase in brightness. To this effect it is referred as to the opposition effect caused by shadow hiding and coherent backscattering and can be observed for most of the asteroids [2].

1.2 Artificial objects

Extensive research has been conducted in last two decades concerning the phase functions of Resident Space Objects (RSOs). It covered the laboratory measurements of representative samples [3], [4], [5] simulation and modelling [6], and most importantly for this study it contained observations acquisition and data fitting [6], [7], [5]. In work [5] authors focus on the improvement of the accuracy of size calculations for optical data by developing optical-based size estimation model. Additionally, their work focuses also on the laboratory modeling of phase curves for some representative objects such as models for Lambertian sphere and cylinder, or real samples of Multi-Layer Insulation (MLI) fragmentation debris. In their work [4], authors proposed using the laboratory testing of their empirical light scattering model for the small debris objects created during the fragmentation. Large amount of space representative materials has been studied in laboratory by [3]. Authors investigated albedo, colors and phase curves of solar cells, white paint, fabrics, glass fabrics and mylar.

2. PHOTOMETRIC PHASE FUNCTION OF ARTIFICIAL OBJECTS

In the work [6] authors state that the best way for modelling any type of satellite, artificial space object is the to assume diffuse sphere as a very first approximation. The reasoning is that there is no variation of photometric return with satellite aspect and the brightness is a straightforward deterministic calculation based on the solar phase angle, satellite albedo, and satellite size (spherical diameter). Authors defined following photometric function equation:

$$m_V(R,\phi) = \begin{array}{c} -26.74 \\ -2.5log(A\rho[\beta F_1(\phi)+(1-\beta)F_2(\phi)]) \\ +5log(R) \end{array} \quad (1)$$

Where A [m] is the sphere's cross-sectional area, ρ is the unite-less bond albedo, which is defined as the fraction of incident light scattered in all directions by the surface [8], R is the satellite-observer range [m], β is a unit-less mixing coefficient representing portion of each component in the resulting brightness, $F_1(\alpha)$ and $F_2(\alpha)$ are diffuse and specular sphere phase functions respectively with definition

$$F_1(\phi) = \frac{2}{3\pi^2}[(\pi-\phi)cos(\phi)+sin(\phi)] \quad (2)$$

$$F_2(\phi) = \frac{1}{4\pi} \quad (3)$$

In their work [6] authors also introduced third lunar phase function to be combine with diffused component to improve the fit by also introducing opposition effect which this function carries. Additionally, authors also considered the so-called earthshine, which is illumination of the satellite by the sunlight reflected from the earth. Authors argue that this effect has no or little effect on overall brightness for satellites observed under phase angles ϕ lower than 120°. However, for higher phase angles the earth shine starts to play a role. In our analysis we are focusing on object on Low Earth Orbit (LEO) observed from ground where it is not expect to observe object under such a low or high phase angles and therefore aforementioned effects will not be further considered for the analysis.

3. PHOTOMETRIC CATALOGUES

We performed similar analysis as the one reported in [9]. However, we were focusing on LEO population as opposite to the deep space population analyzed in [9] and we also considered rotation related changes in the analysis which also influences the reported values. We performed our own analysis using mixture phase functions defined by Eq. 1 to real observations obtained and reported by the Mini Mega Tortora (MMT) system operated by the Kazan Federal University [10]. This database contains more than 400 000 light curves (millions of photometric measurements) for more than 10 500 objects by September 2022. Most reported objects are on LEO as can be seen in Fig. 1 where is plotted MMT population (blue) compared to the objects of the Space Debris Light Curve Database (SDLCD) maintained by Comenius University [11] (orange). Plotted is mean altitude above the surface vs orbital inclination and apogee mean altitude vs perigee mean altitude. MMT database does not provide measurement errors nor the measurements to any of the Russian objects, therefore these objects will not be included in this analysis.

The Space Debris Light Curve Database (SDLCD) is database of the Faculty of Mathematics, Physics and Informatics, Comenius University in Bratislava (FMPI) and contains processed data observed at the Astronomical and Geophysical Observatory in Modra, Slovakia. The main catalogued objects are on geosynchronous, eccentric, global navigation satellite system orbits with recent extension toward LEO [12], [13]. The main instrument for the space debris photometric data collection which provided light curves to SDLCD is FMPI's Newtonian design telescope AGO70 with a very thin 700 mm parabolic mirror from Alluna optics supported by gravity actuators. The focal length of the system is 2962.0 mm. The light from the telescope is detected by the CCD camera FLI-ProLine KAF-1001E Grade 1 front-illuminated full frame monochrome CCD Camera with 65 mm shutter and the resolution of 1024x1024 pixels with pixel size 24 mm. The resulting effective field of view is 29.1'x29.1' and pixel's field of view is 1.67"x1.67". The public version of SDLCD (www.sdlcd.space-debris.sk) currently contains 285 light curves for 226 individual objects [11], while the non-public internal version to be released soon contains more than 1900 light curves for 759 individual objects.

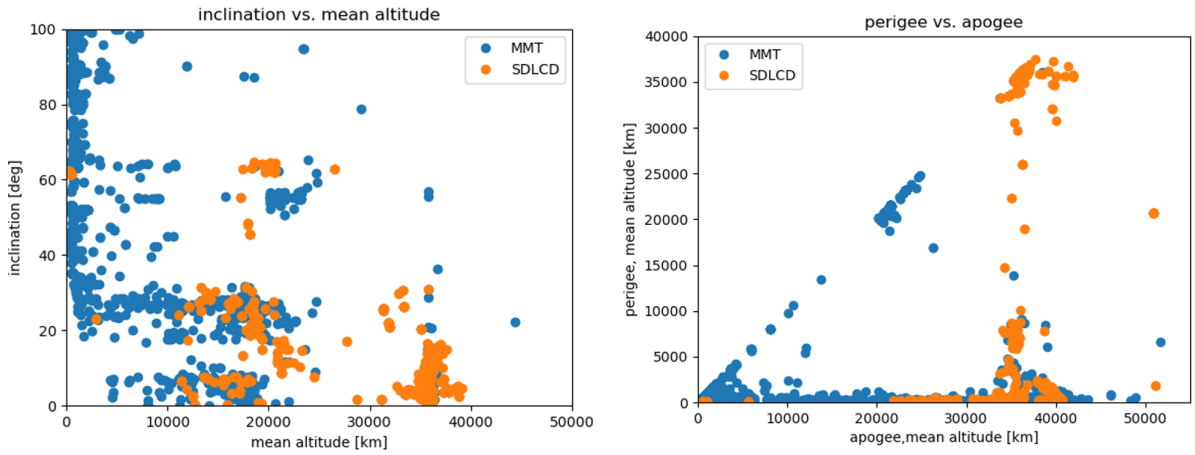

Fig. 1: Orbital elements of objects present in the catalogues MMT (blue) and SDLCD (orange) database.

SDLCD should be considered at the moment as complementary to MMT for the purpose of presented work. SDLCD has its limitations such as that data are not reported in standard magnitude system and database usually contains just a short series for given object during given night, hence it is difficult to construct the phase function. However, it is foreseen to implement in very near future photometric calibration function to the data processing pipeline. SDLCD could be also used occasionally to construct the phase functions as will be discussed in Section 4.2.

4. ESTIMATED PARAMETER OF PHOTOMETRIC FUNCTIONS

4.1 Estimated parameters from MMT database

In this analysis we focused on rotating objects only. The primary objective was to calculate the mean brightness value for a given object and additionally for a given type of population (specific upper stage group, spacecraft etc.). To achieve that we needed to first process the reported photometric measurements provided by MMT. Each file retrieved from MMT database contained the time of observation, reported standard magnitude, reduced magnitude to 1000 km distance, used filter, whether the object was in penumbra, current distance between observer and object [km], phase angle and track identification number. To date 2022-09-26 there were 11492 objects in the database from which 7190 had their photometric measurements available and downloaded for the analysis. Reported are the so-called standard magnitudes in "Clear" magnitude [14]. To obtain the photometric functions of the objects, following steps needed to be performed for all objects for which apparent rotation period has been identified in MMT database:

- a) Standard magnitudes are reduced to 1 AU. This way the absolute magnitude of object H can be directly interpreted as is for the asteroids within the minor planet community. This procedure is demonstrated in Fig. 2 where are plotted brightness measurements of specular sphere Lincoln Calibration Sphere (NORAD 1361, Cospar ID 65034C). Plotted is apparent magnitude as a function of phase angle (left) and reduced apparent magnitude as a function of phase angle (right) which is corrected for the distance. Clearly, some trends were removed, as well the apparent magnitude changed from about 9 mag in average to 31.5 mag in average.
- b) For the rotating object the rotational phase is constructed, and the data is fit with Fourier series of 8^{th} order to cover also small variations in the curve. Extracted is coefficient a_0, representing mean value of the series, which is further used for the analysis. The fit itself provides several coefficients where the most important is a_0 but also amplitude of the signal A_m, which is a difference between the brightest and faintest point of the rotation phase function.
- c) Coefficients a_0 for each rotation curve for given object is plotted into the phase function diagram as shown in Fig. 3.

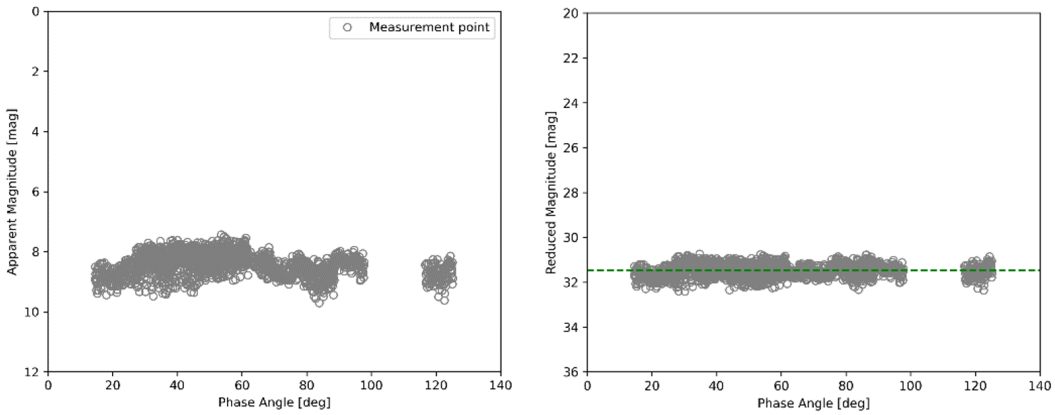

Fig. 2: Apparent magnitude (left) and reduced magnitude distribution after the correction to 1 AU was applied (right) of a random object. Data taken from MMT.

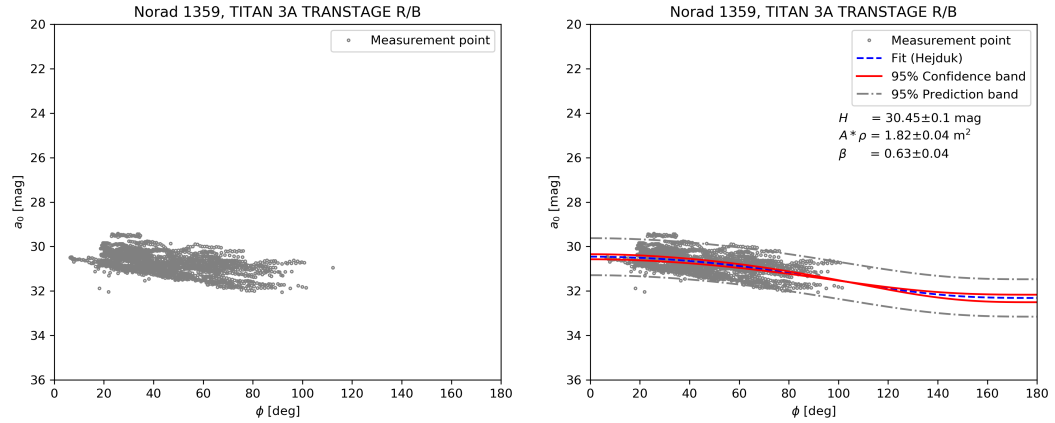

Fig. 3: Left: Phase angle versus coefficient a_0 for object Titan 3A Transtage R/B. Right: Phase angle versus coefficient a_0 for object Titan 3A Transtage R/B including fit (blue line), confidence interval (red line), prediction band (gray dashed line) and estimated parameters.

- d) Coefficients a_0 are fit with mixture phase function using Eq.1, right and extracted are the albedo-area product $A\rho$, coefficient β and consequently absolute magnitude $H = V(1\,AU, 0)$ and corresponding standard deviations. Example of such fit is shown in Fig.3, dashed blue line. For this specific case we estimated $A\rho = 1.82 \pm 0.04\ m^2$, $\beta = 0.63 \pm 0.04$ and $H = 30.45 \pm 0.1\ mag$. Plotted are also boundaries (confidence intervals) defined by the standard deviations of the estimated coefficients marked by solid red lines and prediction bands (gray dashed lines), which contain 95 % of the data points.

In total, there were 7190 objects available in MMT with photometric data where 2741 were identified as rotating with apparent rotation rates available. For each object we calculated coefficients a_0 for each rotational phase, which has been screened for low quality data. Filtered have been phase functions with less than five a_0 points, covering less than 5° in phase angle. In total, 598 objects passed all the filters. Fig. 4 shows the number of measurements points a_0 used for the analysis for given object.

Fig.4 shows the obtained values for parameters $A\rho$, β and H. Detailed analysis showed, that all objects with $A\rho > 100\ m^2$ are large GEO satellites and that all the LEO objects have $A\rho \leq 100\ m^2$. In Fig.4 is shown distribution for values up to $A\rho = 100\ m^2$. More than 81 % of investigated objects had $A\rho \leq 10.0\ m^2$ and more than 33 % of investigated objects had $A\rho \leq 1.0\ m^2$.

For parameter β 37.3 %, showed surface to have highly diffuse behavior having values for β between to 0.9-1.0. For 16.1 % of analyzed objects showed highly specular behavior with β between to 0.0-0.1. The rest of objects, around 54 %, showed mixture of diffuse and specular reflectance which were almost equally redistributed over the interval from 0.1 to 0.9.

Parameter H had values between 25 mag and 37 mag. For most objects (91.2 %) the interval was between 28-34 mag.

There were processed in total 190 objects which could be marked as spacecraft. These objects showed relatively small values for parameter $A\rho$, reaching values up to 10 m^2, where more than 43.7 % has $A\rho \leq 1.0\ m^2$. Parameter β was for 23.2 % of spacecraft objects between to 0.9-1.0, for 18.4 % it was between 0.0-0.1 and there was observed a visible increase in the middle of the interval for values 0.3-0.7. Fig. 5 shows examples of obtained phase functions. Shown are well fitted phase curves for GLOBALSTAR satellite and OPS satellite. There were in total 31 GLOBALSTAR satellites and 8 OPS satellites for which the phase functions were obtained.

There were processed in total 307 objects which could be marked as rocket upper stages. Upper stages showed relatively large parameter $A\rho$, reaching values higher than 10 m^2. Parameter β was for 47.9% of upper stages between to 0.9-1.0, while the rest was almost equally redistributed into the remaining intervals. Examples of obtained phase functions with the confidence intervals are shown in Fig.6. Most of the upper stages had enough measurements thanks to their high visual brightness. While Atlas 5 Centaur R/B shows strong diffuse like reflection, for Electron R/B is visible present strong specular reflection.

There were processed in total 101 objects which could be marked as debris objects. Debris objects showed very small values for parameter $A\rho$, reaching values up to 8 m^2 where most objects had values below 1 m^2 (81.2%). Parameter β is mostly between intervals 0.9-1.0 (31.7%) and 0.0-0.1 (29.7%). Fig. 7 shows examples of obtained phase functions. Shown are well fitted phase curves for Iridium 33 DEB and DELTA 1 R/B DEB. Iridium shows strongly specular reflections, while Delta 1 shows combined behaviour.

4.2 Estimated parameters from SDLCD database

This sections focuses on the construction and analysis of phase function created from the SDLCD data to demonstrate and validate the aforementioned methodology using AGO70 telescope. We conducted observations during the night 15^{th} of June 2023 and the primary targets where objects of SL-6 (2) R/B type. In total, three objects have been observed with COSPAR identifications 74026E (NORAD 7373), 81009D (NORAD 12159) and 85040D (NORAD 15741) using Clear C filter. All objects where of the same build and with age 11 years apart. We extracted instrumental magnitudes for each object and processed the acquired light curves to extract the apparent rotation periods P_{app} using methodology described in [11]. Examples of reconstructed rotational phases using instrumental magnitudes can be seen in Fig. 8. For object 74026E we found $P_{app} = 53.64\ s$, for 81009D we found $P_{app} = 12.06\ s$ and for 85040D $P_{app} = 4.61\ s$.

The extracted instrumental magnitudes were transferred for each object into the standard system of magnitudes using reference stars from the Gaia catalogue [15]. The resulting light curves can be seen in Fig. 9.

We screened the acquired light curves for outliers and we constructed the phase function of SL-6(2) R/B objects using

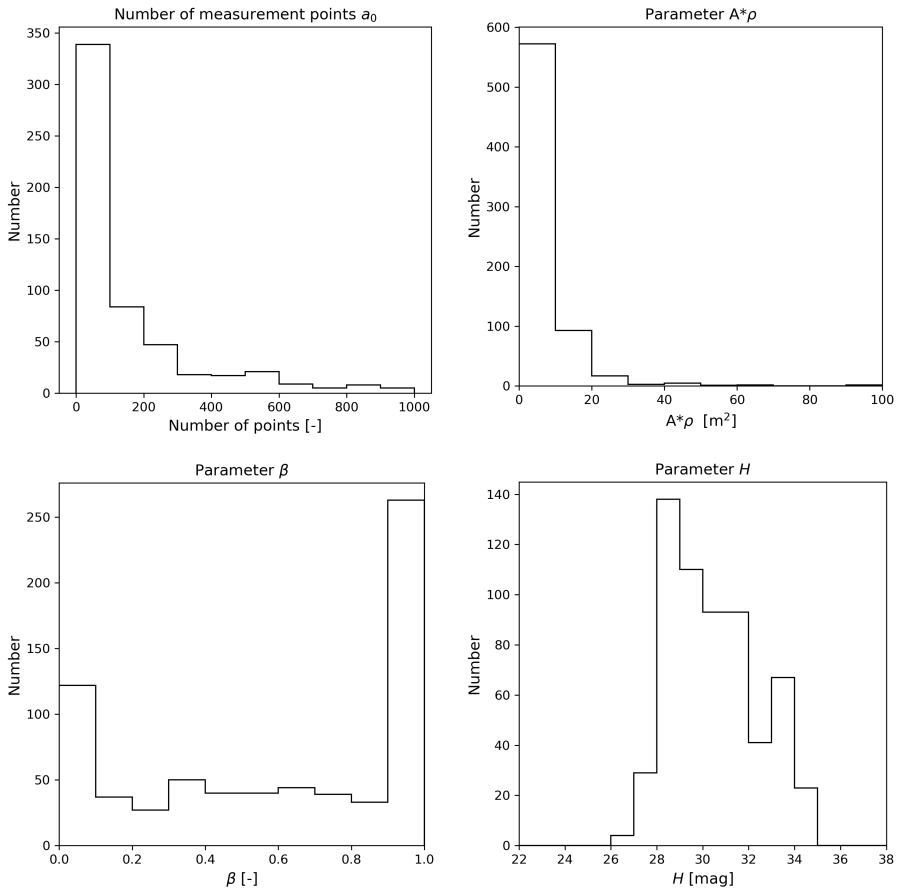

Fig. 4: Number of points used for the analysis (left up), extracted parameters $A\rho$ (right up), β (lower left) and H (lower right) analyzing 598 objects from MMT database.

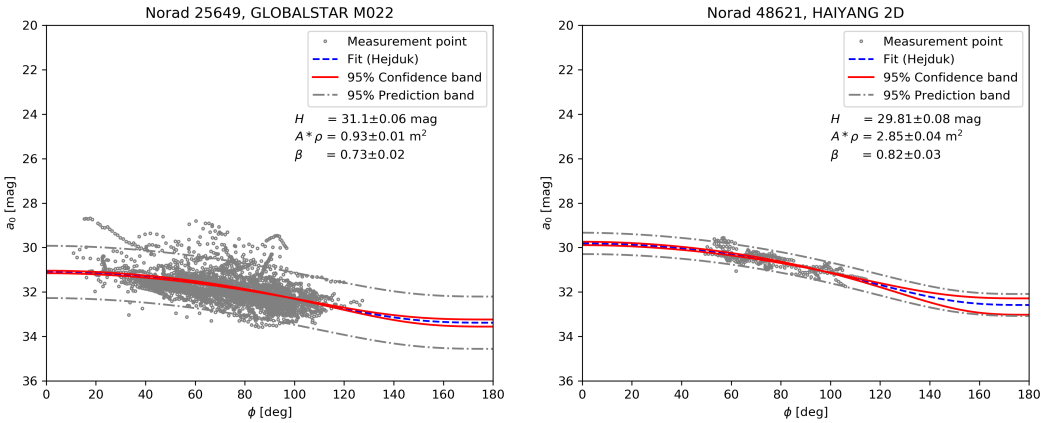

Fig. 5: Examples of well fitted phase curves for spacecraft. Shown are Globastar M022 (left) and OPS 5644 (right).

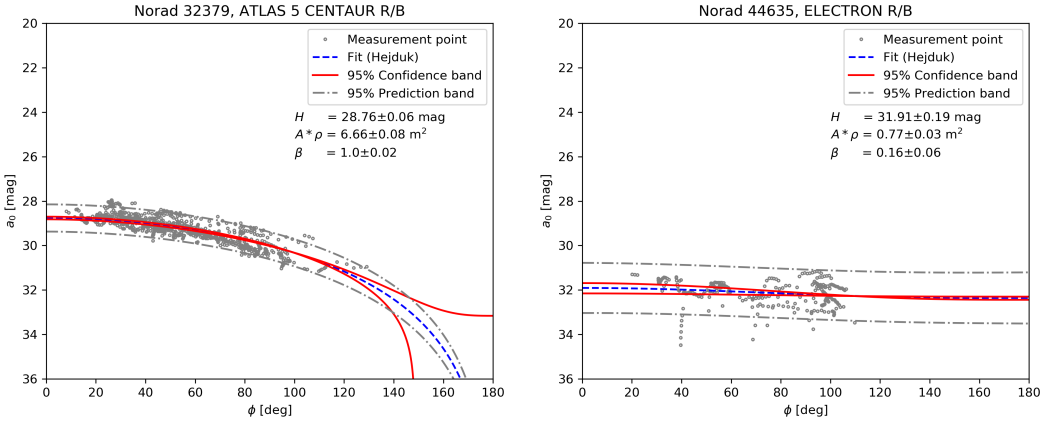

Fig. 6: Examples of well fitted phase curves for upper stages. Shown are Atlas 5 Centaur R/B (left) and Electron R/B (right).

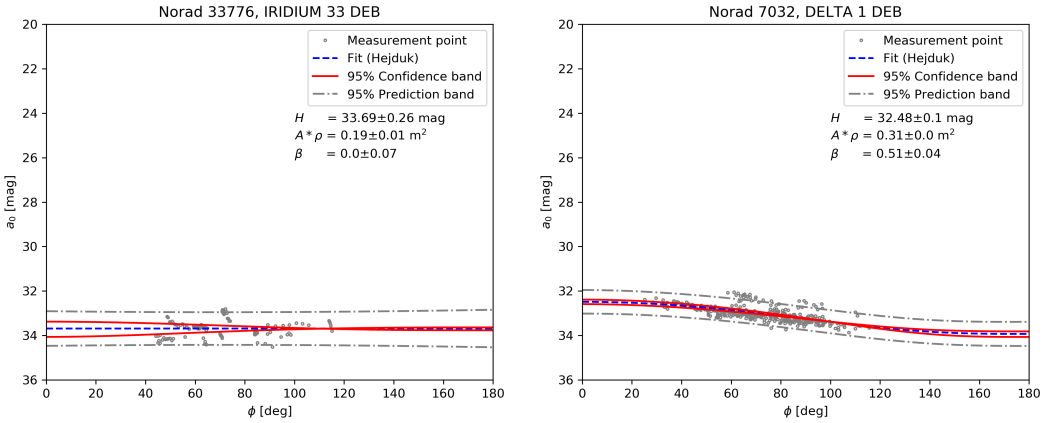

Fig. 7: Examples of well fitted phase curves for space debris objects. Shown are fragments of Iridium 33 satellite (left) and of Delta 1 upper stage (right).

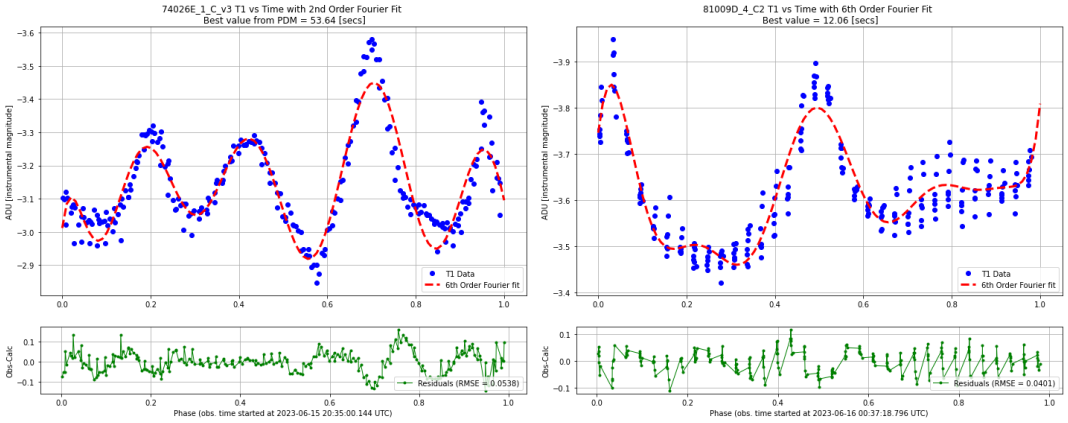

Fig. 8: Reconstructed rotational phases for objects 74026E (first series) and 81009D (fourth series) in instrumental magnitude system.

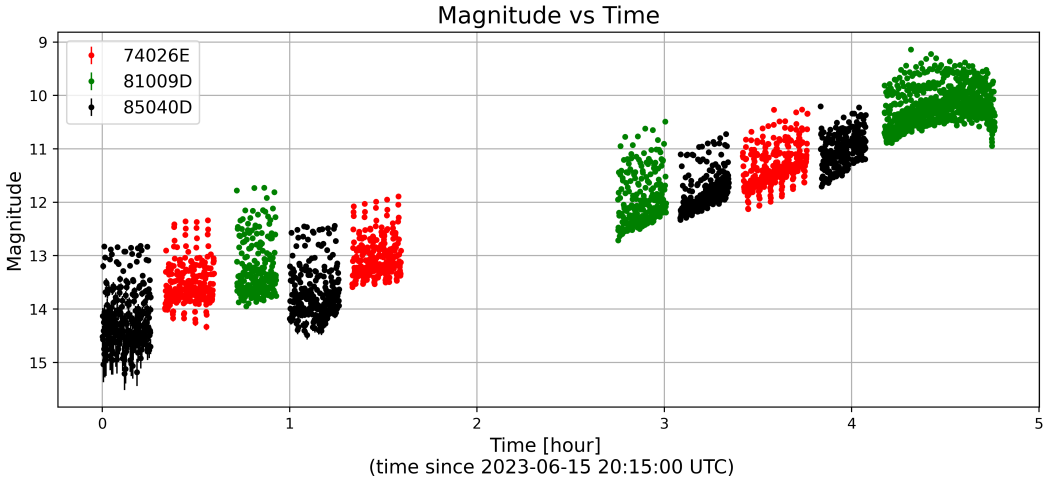

Fig. 9: Light curves of objects 74026E (NORAD 7373), 81009D (NORAD 12159) and 85040D (NORAD 15741) in standard magnitude system acquired with AGO70 telescope during night 20230615 using C filter and exposure of 1 s.

methodology described in Section 4.1. The resulting diagram can be seen in Fig. 10. For this type of population we got $\beta_c = 0.74 \pm 0.05$ which is highly diffuse type of reflection. For parameters H_c and $A\rho_c$ we got $H_c = 30.36 \pm 0.12$ *mag* and $A\rho_c = 1.83 \pm 0.06$ m^2 which is close to values of Titan 3A Transtage R/B presented in Fig.3.

5. GEOMETRIC ALBEDO ESTIMATION

Previous analysis was focusing on the photometric properties of the RSOs, not much revealing about their physical properties. Parameter $A\rho$ contains information about the objects geometric albedo as well the mean cross section. Once the latter is known, it is possible to layout hypothesis about object's cross section observed during data acquisition, hence it is possible to estimate ρ. For upper stages, for which we assume hereafter perfect cylinder, it is reasonable to assume that upper stage is rotating about the transverse axis through its center of mass [16]. For simplicity, if we assume that no precession and nutation are present, these objects are the brightest for a given observer and a given phase angle when the curved surface of the upper stage is facing the observer, hence the line-of-sight (LoS) is parallel to the axis of rotation. At that moment the observer only sees or receives the light from the curved surface of the cylinder and the base is not contributing. Therefore, the maximum of area A_{max} is reflecting the light toward the observer when maximum brightness is detected for given phase angle and the mean area A_{mean} is reflecting the light when the mean brightness is observed [17]. As an example case we selected object of Titan 3A Transtage R/B (82040C, 1359) which phase function is plotted in Fig. 3. Object has a raw surface dominated by the aluminum alloy or it is covered by the aluminum-based paint [18]. It is cylindrical object with height of 4.57 m and diameter of 3.05 m [16], [18] with maximum cross section $A_{max} = 15.66$ m^2 and mean cross section $A_{mean} = 14.47$ m^2 calculated using ESA DRAMA (Debris Risk Assessment and Mitigation Analysis) tool functionality CROC (Cross-section Of Complex Bodies) [19]. Titan 3A Transtage R/B has $A\rho = 1.82$ m^2 and mixed reflective properties with $\beta = 0.63$. The maximum and minimum prediction bands for this object were estimated to be $Pr_{A\rho,max} = 3.92$ m^2 and $Pr_{A\rho,min} = 0.84$ m^2 respectively.

Once all the data are available, it was possible to calculate the geometric albedo for scenario when maximum cross section was facing toward the observer $\rho_{max} = Pr_{A\rho,max}/A_{max}$ and when the mean cross section was facing the observer $\rho_{mean} = A\rho/A_{mean}$. For Titan 3A Transtage R/B we measured $\rho_{max} = 25.04$ %, which could be expected for object covered by a mate aluminum-based paint. Once we look at the calculated mean value $\rho_{mean} = 12.58$ % the geometric albedo suddenly drops significantly. It is clear that this is caused by the contribution from both bases to the overall brightness (mean brightness for which we calculated parameter $A\rho$) and that probably the shadowing effect plays a role.

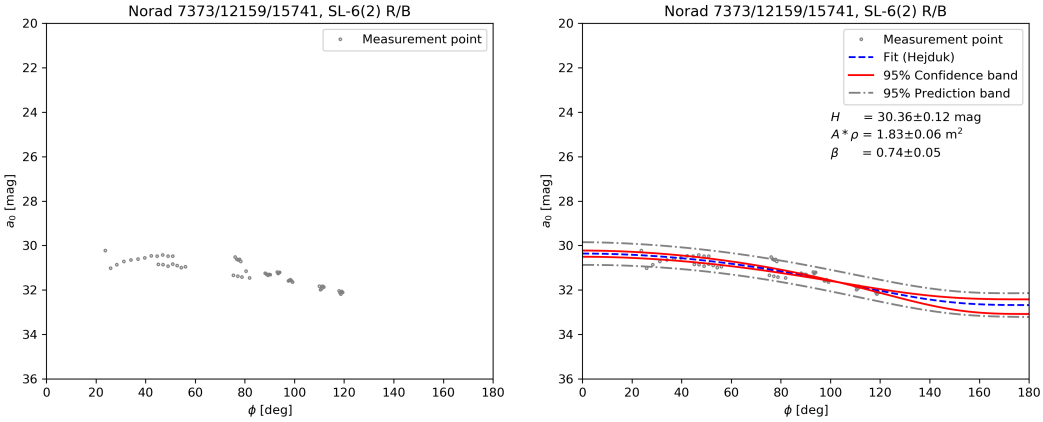

Fig. 10: Left: Photometric measurements of objects 74026E, 81009D and 85040D using representative average a_0 values. Right: Phase function of SL-6(2) R/B objects 74026E and 81009D and 85040D.

6. SUMMARY AND CONCLUSIONS

In our work we presented properties of photometric phase functions obtained for almost 600 individual objects using publicly available photometric data collected in last 8 years by the Mini Mega Tortora (MMT) system utilizing the methodology introduced by [6]. Phase function contain information about the reflectance properties of the RSOs, as well their physical properties such as geometric albedo ρ and area A. In the work we report properties of the surface diffusion represented by the parameter β and the physical properties represented by parameter $A\rho$ or absolute magnitude H. We found out that more than 81% of investigated objects had $A\rho \leq 10.0\ m^2$ and more than 33% of investigated objects had $A\rho \leq 1.0\ m^2$. For parameter β, 37.3% of objects had surface with highly diffuse behavior having values for β between to 0.9-1.0. Around 16.1% of analyzed objects showed highly specular behavior with β between to 0.0-0.1. The rest of objects, around 54%, showed mixture of diffuse and specular reflectance. Parameter H had values between 25 mag and 37 mag. For most objects (91.2%) the interval was between 28-34 mag.

Objects which could be marked as spacecraft showed relatively small values for parameter $A\rho$, reaching values up to 10 m^2, while upper stages reached $A\rho$ also above up 10 m^2. Space debris objects represented by fragmentation and mission-related debris where dominantly with $A\rho$ less than 1 m^2 (81.2%). For spacecraft population parameter β was redistributed between the whole interval 0.0 to 1.0 with small maxima close to fully diffuse like reflection and mirror/specular-like reflection. For upper stages the dominant was diffuse-like reflection where 47.9% of upper stages had β between 0.9-1.0. Debris objects showed dominantly diffuse- or specular-like reflection with similar representation.

Using the estimate parameters of phase function we also estimated geometric albedo of one selected upper stage Titan 3A Transtarge R/B for which we estimated geometric albedo for two scenarios, maximum cross section is visible from the perspective of observer and mean cross section is visible from the observer. We calculated relatively low values $\rho_{max} = 25.04$ % and $\rho_{mean} = 12.58$ %, which could be expected for object covered by a mate aluminum-based paint.

Additionally, we also successfully demonstrated the phase function construction methodology on data acquired by our own telescope AGO70. Observed were three objects from SL-6(2) R/B group during one photometric night. For this type of population we got $\beta_c = 0.74 \pm 0.05$ which is highly diffuse type of reflection. For parameters H_c and $A\rho_c$ we got $H_c = 30.36 \pm 0.12\ mag$ and $A\rho_c = 1.83 \pm 0.06\ m^2$ respectively. Used method and observation campaign will be extended to investigate different groups of family objects on LEO, GEO and deep space objects as well to investigate unknown debris objects to support their characterization along the color photometry [17] and spectroscopy [20] utilized at Comenius University in Bratislava.

ACKNOWLEDGMENTS

This work has been supported by ESA project under the 7^{th} call of Plan for European Cooperating States in Slovakia with Contract no. *4000139802/22/NL/SC - Modelling the night sky brightness produced by space objects*.

7. REFERENCES

[1] K. Muinonen and et al. A three-parameter magnitude phase function for asteroids. *Icarus*, 209(2):542–555, 2010.

[2] I.N. Belskaya and V.G. Shevchenko. Opposition effect of asteroids. *Icarus*, 147(1):94–105, 2000.

[3] A. Murtazov. Comparison between space debris and asteroids' photometric properties. In *Proceedings of the Asteroids, Comets, Meteors, Helsinki, Finland*, 2014.

[4] J. Peltoniemi and et al. Light scattering model for small space debris particles. *Advances in space research*, 70(10):2961–2975, 2022.

[5] J. Hostetler and H. Cowardin. Experimentally-derived phase function approximations in support of the orbital debris program office. In *Proceedings of the First International Orbital Debris Conference, Houston, USA*, 2019.

[6] Hejduk M. Specular and diffuse components in spherical satellite photometric modeling. In *Proceedings of AMOS Conference, held in Wailea, Maui, Hawaii, September 13-16, 2011*, 2011.

[7] J. Africano and et al. Understanding photometric phase angle corrections. In *Proceedings of the 4th European Conference on Space Debris, 18-20 April 2005*, 2005.

[8] S.M. Lederer and et al. The 2004 Las Campanas/Lowell Observatory campaign II. surface properties of Hayabusa target asteroid 25143 Itokawa inferred from Hapke modeling. volume 60, pages 49–59. Springer Science & Business Media, 2008.

[9] Hejduk M. Satellite material type and phase function determination in support of orbital debris size estimation. In *Proceedings of the Advanced Maui Optical and Space Surveillance Technologies Conference, held in Wailea, Maui, Hawaii, September 11-14, 2012*, 2012.

[10] Karpov S. Massive photometry of low-altitude artificial satellites on Mini-Mega-TORTORA. In *Proceedings of the IV Workshop on Robotic Autonomous Observatories, Revista Mexicana de Astronomía y Astrofísica (Serie de Conferencias) Vol. 48, pp. 112-113, 2016*, 2016.

[11] Šilha J. et al. Space debris observations with the Slovak AGO70 telescope: Astrometry and light curves. *Advances in Space Research*, 65(8):2018–2035, 2020.

[12] J. Šilha and et al. AGO70: passive optical system to support SLR tracking of space debris on LEO. In *Proceedings of the Advanced Maui Optical and Space Surveillance Technologies Conference, held in Wailea, Maui, Hawaii, 2021*, 2021.

[13] J. Šilha and et al. Development and operational status of AGO70 telescope. In *Proceedings of the 8th European Conference on Space Debris, Darmstadt, Germany*, 2021.

[14] A. Mallama and D. Anthony. Starlink satellite brightness – characterized from 100,000 visible light magnitudes. *arXiv preprint arXiv:2111.09735*, 2021.

[15] Riello, M. and et al. Gaia early data release 3 - photometric content and validation. *Astronomy & Astrophysics*, 649:A3, 2021.

[16] Astronautix. Titan 3A rocket properties. In *http://www.astronautix.com/t/titaniiia.html*, 2023.

[17] Zigo M., Šilha J., Hrobár T., and Jevčák P. Space debris surface characterization through BVRI photometry. *Advances in Space Research*, 2023.

[18] H. Cowardin and et. al. Characterizing GEO Titan IIIC Transtage fragmentations using ground-based and telescopic measurements. In *Proceedings of the Advanced Maui Optical and Space Surveillance Technologies Conference, held in Wailea, Maui, Hawaii, 2017*, 2017.

[19] Oikonomidou X. and et al. Guidelines for space debris and meteoroid impact risk assessment with DRAMA/MIDAS. In *Proceedings of the 8th European Conference on Space Debris, 2021*, 2005.

[20] Žilková D., Šilha J., Matlovič P., and Tóth J. Space debris spectroscopy: Specular reflections at LEO regime. *Advances in Space Research*, 71(8):3249–3261, 2023.